



*Supplement of*

## **Spatially and temporally resolved measurements of $\text{NO}_x$ fluxes by airborne eddy covariance over Greater London**

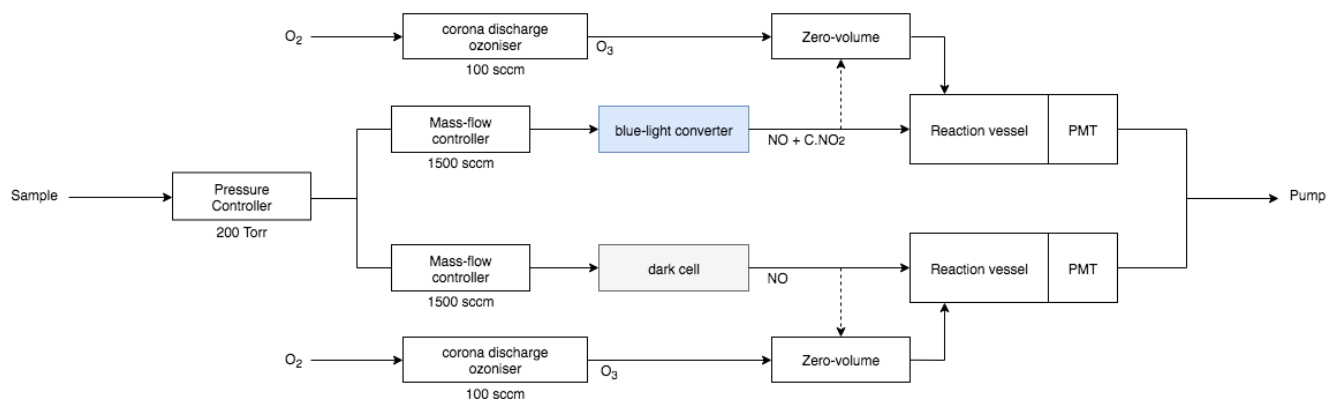
**Adam R. Vaughan et al.**

*Correspondence to:* Adam R. Vaughan ([adam.vaughan@york.ac.uk](mailto:adam.vaughan@york.ac.uk))

The copyright of individual parts of the supplement might differ from the article licence.

## Supplementary Information

### S1.1 Instrument information



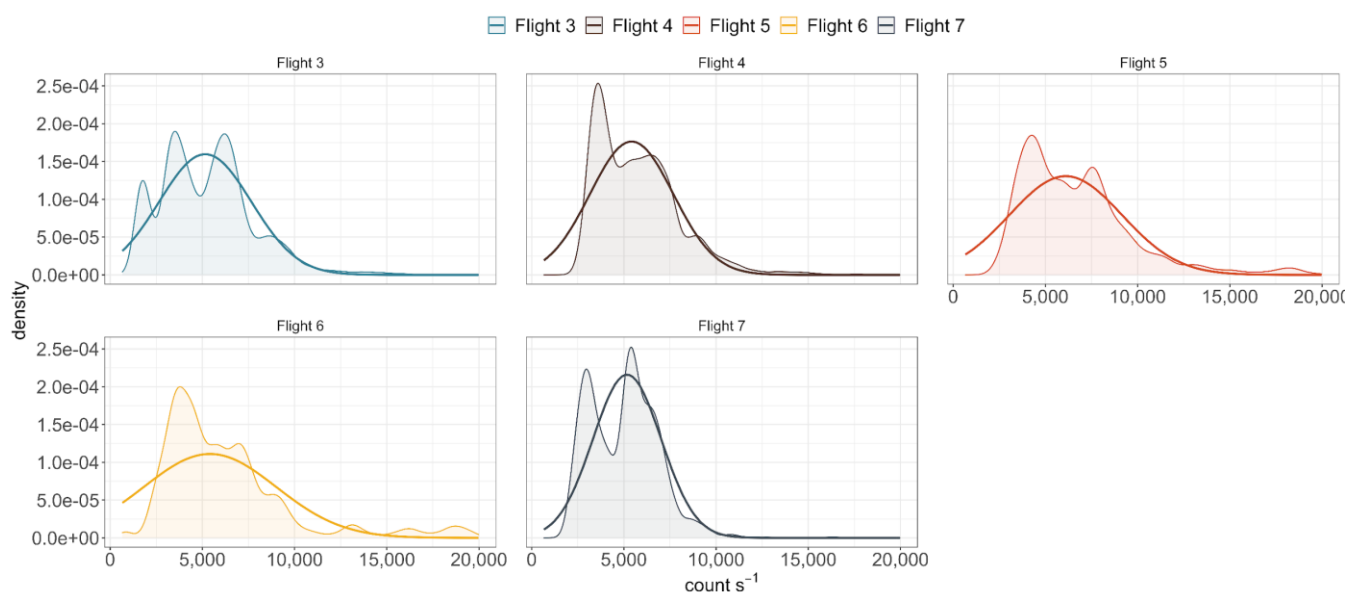
**Figure S1. Instrument schematic for fast AQD dual-channel chemiluminescence NO<sub>x</sub> analyser (Fast-AQD-NO<sub>x</sub>). Dotted flow path represents zero count-rate flow path for both channels, giving a zero-count rate for each PMT.**

Fig. 1S depicts the flow schematic for the instrument, showing two separate detection channels for NO and NO<sub>2</sub>. Sample inlet pressure is kept at >300 hPa to negate the effect of changing altitude on instrument sensitivity. The blue-light converter consists of a Teflon block containing a milled cavity (10 mL volume) down its centre, and three 395 ± 20 nm wavelength LED positioned on either side (Reed et al., 2016). Below 400 nm NO<sub>2</sub> photolytically degrades to NO and ground-state molecular oxygen (O[<sup>3</sup>P]). The converter is cooled using a Peltier cooler to reduce thermal interference products and exhibits a conversion efficiency of >85 % and a resonance time of 0.11 s.

The dark count rate on each PMT was assessed using the zero-volume flow path shown in Fig. 1s as the dotted line. Mixing between the sample flow and O<sub>3</sub> occurs in the zero-volume, ensuring the chemiluminescence reaction occurs before the sample reaches the reaction vessel. Typical PMT dark counts ranged from 2,000-6,000 counts s<sup>-1</sup>. The dark-count rate on each PMT was measured frequently and subtracted from the ambient signal to give an accurate background correction. Instrument design takes into account water vapour quenching with regards to photon counting (Ridley et al., 1992). A constant amount of deionised water vapour (d.H<sub>2</sub>O) is added to the O<sub>3</sub> supply, increasing the concentration within the reaction vessel to ~32 parts per thousand (ppth). By standardising water vapour within the reaction vessel, any changes in atmospheric water vapour concentration are negated which negates significant chemiluminescence quenching effects.

The sensitivities of both the PMTs and the blue-light converter can drift over time, requiring calibration to a known NO/NO<sub>2</sub> standard. A 5 ppm NO standard (BOC Group plc., supplied and certified) was used to calibrate against, which was further

certified against a high accuracy National Physical Laboratory (NPL) standard, before and after the field campaign. Instrument mass-flow controllers were calibrated before and after field campaigns using a gilibrator (high accuracy electric bubble flow meter). PMT sensitivity was determined by standard addition of a small flow (5 - 10 sccm) of NO calibrant gas to a flow of NO<sub>x</sub>-free air. NO<sub>x</sub> free air was obtained either by flying above the boundary layer where NO<sub>x</sub> levels are low or by removal using a Sofnofil/charcoal trap attached to the sample inlet. This gave a NO mixing ratio in the range 5 – 10 ppt. NO channel sensitivity values range from 7 - 8 counts ppt<sup>-1</sup>. NO<sub>2</sub> detector sensitivity was also determined by the same method, with typical value ranges from 9 - 11 counts ppt<sup>-1</sup>. In addition to detector sensitivity, the conversion efficiency of the blue-light converter was also assessed. A known NO<sub>2</sub> mixing ratio was generated by titration reaction of NO calibrant gas with O<sub>3</sub>, generated by a 5 sccm flow of O<sub>2</sub> passing by a 254 nm Oriel Instruments Mercury UV Pen-Ray lamp. The converter was found to give > 85% conversion efficiency during the entire campaign.



**Figure S2.** The density distribution (shaded area) of in-flight zero counts for each individual flight throughout the campaign. The calculated normalised gaussian distribution shown as the solid Line.

## S1.2 Eddy Covariance and Quality Metrics

### S1.2.1 eddy4R Software

The eddy4R software is a family of R packages (Core Team, 2019) which create a modular function-based software solution for EC data processing, as described in Metzger et al., (2017). A development and systems operation approach (DevOps) was utilised to create reproducible, open-source, and extensible software that is version controlled. This DevOps schema enables a release and iteration cycle that, to date, has yielded the eddy4R.base, eddy4R.qaqc, and eddy4R.stor packages on a publicly available GitHub repository (Metzger et al., 2019; Xu et al., 2019). This modular framework facilitates scientific community-driven code development that extends the eddy4R software suite’s capabilities. In the present study, we extended eddy4R to handle fluxes from a wide variety of chemical species by adding to the eddy4R.turb package that is currently in development.

To ensure portability and reproducibility, the eddy4R packages integrate into a Docker image, which builds upon a Linux computational environment and resolves all system and R dependencies (<https://www.docker.com/why-docker>). The Docker image hardens the code against operating system-induced anomalies and streamlines the code base to the essential requirements for processing. GitHub automatically triggers, and version controls Docker image builds, which are housed on Dockerhub. Continuous integration testing through Travis-CI and subsequent code reviews complete the build chain. This fosters rapid code development across teams and functionalities while mitigating unintentional errors that could corrupt the main codebase. The eddy4R-Docker DevOps framework thus provides a foundation for the distributed development of novel algorithmic solutions and their scalable execution. The described approach provides the end-user with a practical approach towards version control and result reproducibility.

### S1.2.2 Wavelet Eddy Covariance

Wavelet EC uses continuous wavelet transformation (CWT) to extract time-frequency or space-wavenumber information from atmospheric signals. For this study, the Morlet wavelet (Cohen, 2019) was chosen due to its strong track record in quantifying atmospheric turbulence (Karl et al., 2013; Thomas and Foken, 2005). The complete covariance between two signals ( $x$  &  $y$ ) is deduced by examining global covariance across all frequency scales, as shown in Eq. (1).  $a_j$  defines the frequency domain scales,  $b_n$  the time-domain scales,  $\delta t$  the steps between time-domain scales,  $\delta j$  the spacing between frequency domain scales, length of the data series ( $N$ ) and  $C_\delta$  wavelet specific reconstruction factor. CWT frequency scales are chosen so that the smallest resolvable scale ( $s_0$ ) is equal to  $2\delta t$  (half sampling frequency) and the largest scale being  $\delta j^{-1} \log_2(N\delta t/s_0)$ . During CWT, the wavelet is scaled in both frequency and time domains, using a defined number of scales, Eq. (2-3). Frequency-domain scales increase exponentially from  $j = 0$  to  $J$  ( $J$  being the Nyquist frequency). Time-domain scales are increased linearly, from  $n = 0$  to  $N-1$  ( $N$  equal to the length of data series). A  $\delta j$  value of 1/8 was chosen as a compromise between high-frequency resolution without long computational time. The average frequency-resolved coefficients over a selected segment of time give a real covariance between two signals, which in turn is used to calculate the eddy-flux (Metzger et al., 2013). Summatively, this approach provides localised highly resolved fluxes whilst accounting for all relevant transport scales.

$$F = \overline{x'y'} = \frac{\delta j \delta t}{C_{\delta} N} \sum_{j=0}^J \sum_{n=0}^{N-1} \frac{w_x(a_j, b_n) w_y(a_j, b_n)^*}{a_j}, \quad (1)$$

$$a_j = a_0 2^{j \delta j}, \quad (2)$$

$$b_n = n \delta t, \quad (3)$$

### 1.2.2 Eddy Covariance Quality Metrics

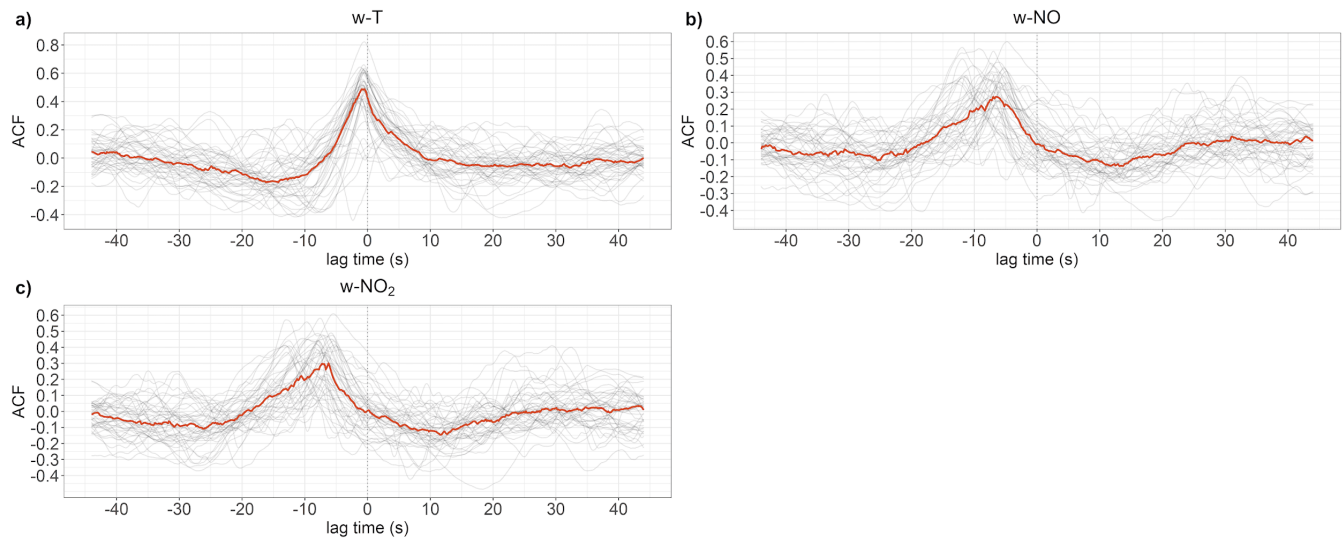


**Figure S3. Individual flight leg time cross-correlation plots for temperature (a), NO (b) and NO<sub>2</sub> (c) against vertical wind as the reference. The median fit across the cross-correlation is shown in red.**

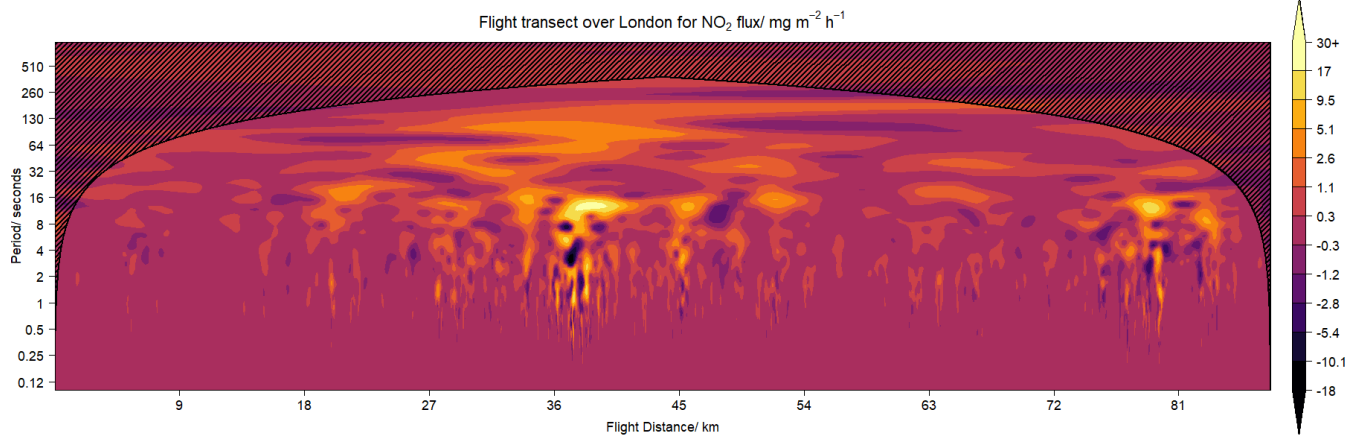


**Figure S4.** Example wavelet cross-scalogram for  $\text{NO}_2$  flux along a flight transect over Central London. Warm colours showing areas of emission and cooler colours deposition. Shaded region presenting the wavelet cone of influence.

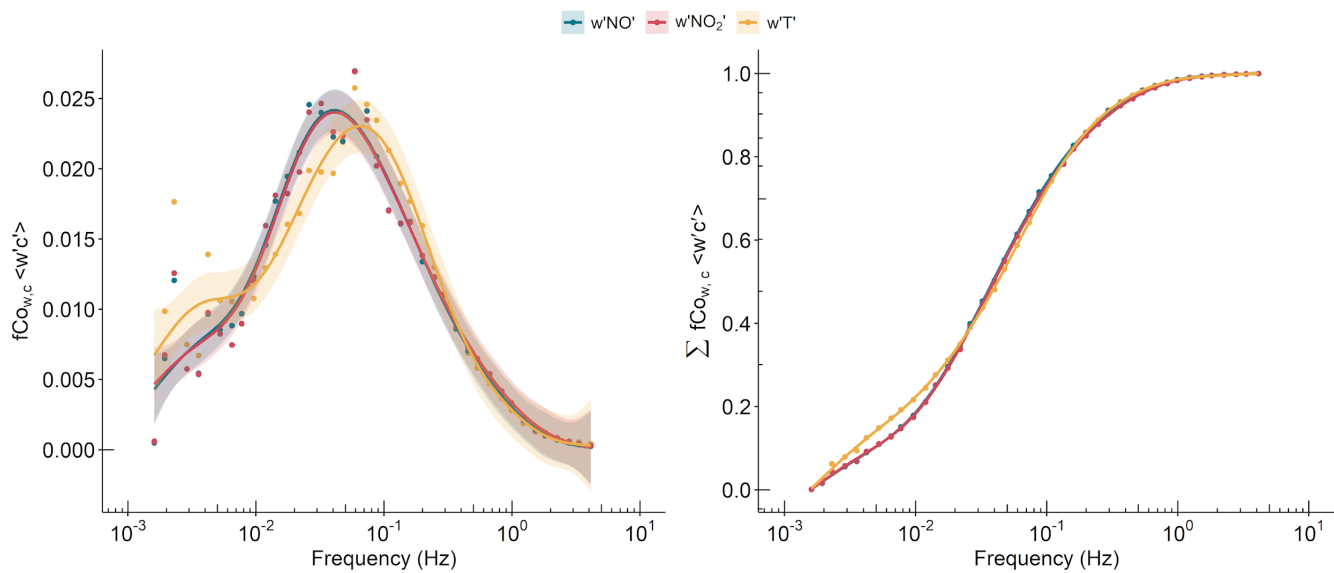


**Figure S5.** Average co-spectra (a) and cumulative co-spectra (b) for fluxes of NO,  $\text{NO}_2$  and latent heat.

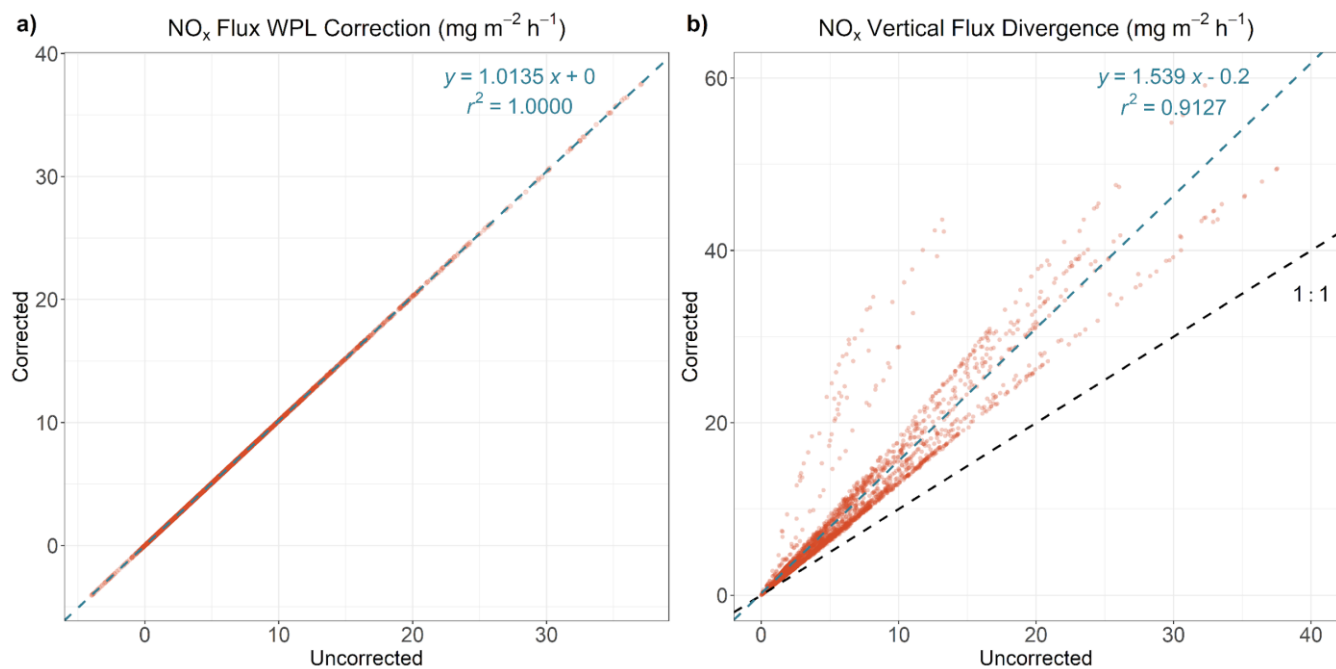


**Figure S6. a) NO<sub>x</sub> flux density correction (WPL) with linear regression in blue, using the method described in Hartmann et al., 2018, Eq.21. b) NO<sub>x</sub> flux vertical flux divergence correction (Deardorff, 1974; Sorbjan, 2006), with linear regression in blue and 1:1 line in black.**

### 1.3 Boosted Regression Model Metrics

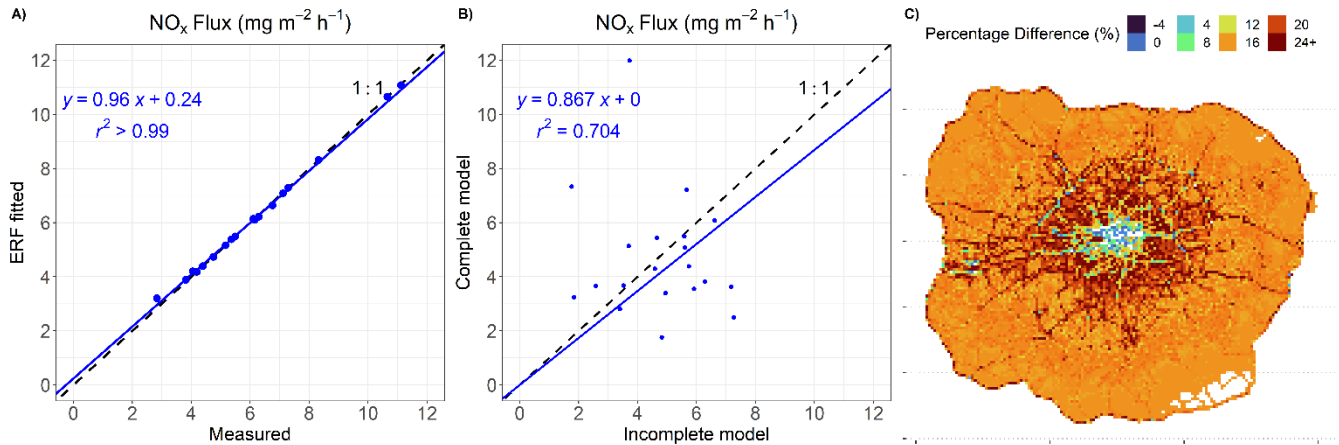


**Figure S7. A) linear regression between the average (median) flight transect measured vs BRT predicted NO<sub>x</sub> flux. B) linear regression between the average (median) flight transect NO<sub>x</sub> flux using an incomplete BRT model to predict the transect vs the complete BRT model. C) The spatial percentage difference between the average (median) flight transect projection compared to the average projection using an incomplete model to predict the transect. Positive values represent higher predicted emissions by the incomplete model. Negative values represent an underprediction of emissions by the incomplete model.**

Individual Projections (mg m<sup>-2</sup> h<sup>-1</sup>)

4	6	8	10	12	14	16	18	20+
---	---	---	----	----	----	----	----	-----

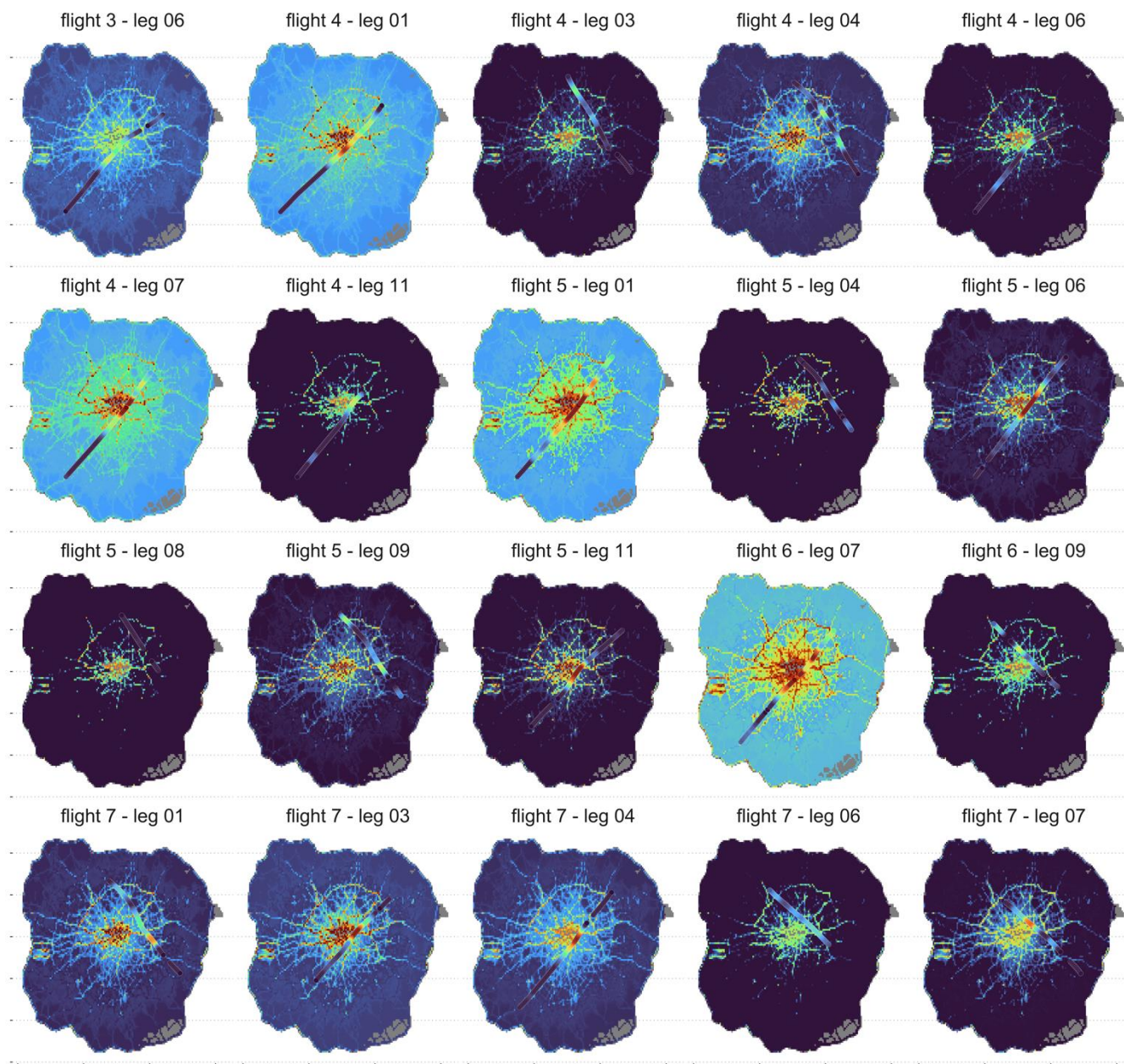


**Figure S8. Individual ERF flight transect projections for the Greater London Region using median average statistics, with measured NO<sub>x</sub> fluxes along each transect shown as the dotted points.**

## References

- Cohen, M. X.: A better way to define and describe Morlet wavelets for time-frequency analysis, *Neuroimage*, 199, 81–86, doi:<https://doi.org/10.1016/j.neuroimage.2019.05.048>, 2019.
- Core Team, R.: R: A language and environment for statistical computing, R Found. Stat. Comput. Vienna, 2019.
- Deardorff, J. W.: Three-dimensional numerical study of turbulence in an entraining mixed layer, *Boundary-Layer Meteorol.*, 7(2), 199–226, 1974.
- Hartmann, J., Gehrman, M., Kohnert, K., Metzger, S. and Sachs, T.: New calibration procedures for airborne turbulence measurements and accuracy of the methane fluxes during the AirMeth campaigns, *Atmos. Meas. Tech.*, 11(7), 4567–4581, doi:10.5194/amt-11-4567-2018, 2018.
- Karl, T., Misztal, P. K., Jonsson, H. H., Shertz, S., Goldstein, A. H. and Guenther, A. B.: Airborne Flux Measurements of BVOCs above Californian Oak Forests: Experimental Investigation of Surface and Entrainment Fluxes, OH Densities, and Damkohler Numbers, *J. Atmos. Sci.*, 70(10), 3277–3287, doi:Doi 10.1175/Jas-D-13-054.1, 2013.
- Metzger, S., Junkermann, W., Mauder, M., Butterbach-Bahl, K., Widemann, B. T. Y., Neidl, F., Schafer, K., Wieneke, S., Zheng, X. H., Schmid, H. P. and Foken, T.: Spatially explicit regionalization of airborne flux measurements using environmental response functions, *Biogeosciences*, 10(4), 2193–2217, doi:DOI 10.5194/bg-10-2193-2013, 2013.
- Metzger, S., Durden, D., Sturtevant, C., Luo, H., Pingingtha-Durden, N., Sachs, T., Serafimovich, A., Hartmann, J., Li, J. and Xu, K.: eddy4R 0.2. 0: a DevOps model for community-extensible processing and analysis of eddy-covariance data based on R, Git, Docker, and HDF5, *Geosci. Model Dev.*, 10(9), 3189, 2017.
- Metzger, S., Ayres, E., Durden, D., Florian, C., Lee, R., Lunch, C., Luo, H., Pingingtha-Durden, N., Roberti, J. A. and Sanclements, M.: From NEON field sites to data portal: a community resource for surface-atmosphere research comes online, *Bull. Am. Meteorol. Soc.*, (2019), 2019.
- Reed, C., Evans, M. J., Carlo, P. D., Lee, J. D. and Carpenter, L. J.: Interferences in photolytic NO<sub>2</sub> measurements: explanation for an apparent missing oxidant?, *Atmos. Chem. Phys.*, 16(7), 4707–4724, 2016.
- Ridley, B. A., Grahek, F. E. and Walega, J. G.: A small high-sensitivity, medium-response ozone detector suitable for measurements from light aircraft, *J. Atmos. Ocean. Technol.*, 9(2), 142–148, 1992.
- Sorbjan, Z.: Statistics of scalar fields in the atmospheric boundary layer based on large-eddy simulations. Part II: Forced convection, *Boundary-layer Meteorol.*, 119(1), 57–79, 2006.
- Thomas, C. and Foken, T.: Detection of long-term coherent exchange over spruce forest using wavelet analysis, *Theor. Appl. Climatol.*, 80(2), 91–104, 2005.
- Xu, K., Pingingtha-Durden, N., Luo, H., Durden, D., Sturtevant, C., Desai, A. R., Florian, C. and Metzger, S.: The eddy-covariance storage term in air: Consistent community resources improve flux measurement reliability, *Agric. For. Meteorol.*, 279, 107734, 2019.